Univerzita Karlova
Přírodovědecká fakulta

Studijní program: Chemie
Studijní obor: Anorganická Chemie

Bc. Pavlína Nedvědová Šolcová

Příprava a vlastnosti karbidů přechodných kovů

DIPLOMOVÁ PRÁCE

Školitel: RNDr. Václav Tyrpekl, Ph.D.
Konzultantka: Ing. Petra Ecorchard, Ph.D.

Praha 2023

Charles University

Faculty of Science

Study programme: Chemistry

Branch of study: Inorganic Chemistry

Bc. Pavlína Nedvědová Šolcová

Synthesis and properties of transition metal carbides

DIPLOMA THESIS

Supervisor: RNDr. Václav Tyrpekl, Ph.D.

Tutor: Ing. Petra Ecorchard, Ph.D.

Prague 2023

Prohlášení:

Prohlašuji, že jsem závěrečnou práci zpracovala samostatně a že jsem uvedla všechny použité informační zdroje a literaturu. Tato práce ani její podstatná část nebyla předložena k získání jiného nebo stejného akademického titulu.

V Praze, 15. 5. 2023

Podpis

Abstrakt

Tato diplomová práce navazuje na můj bakalářský projekt, ve kterém jsem úspěšně připravila karbid s vysokou entropií (HEC) o složení (Ti, Zr, Hf, Nb, Ta)C roztokovou metodou následovanou karbotermální redukcí pomocí metody *Spark plasma sintering* (*SPS)*. Hlavní cíle této práce se dají rozdělit do tří etap. První etapou bylo využití metody *Ultrafast high-temperature sintering (UHS)* pro přípravu vysokoentropického karbidu (Ti, Zr, Hf, Nb, Ta)C namísto SPS. Hlavními výhodami *UHS* oproti *SPS* jsou až tisíckrát menší spotřeba elektrické energie a jednodušší instrumentace. Druhou etapou bylo testování této syntetické metody na karbidu o jiném složení, v tomto případě (Cr, Mn, Fe, Co, Ni)C. Třetí etapou bylo studium možnosti použití této roztokové metody a *UHS* na přípravu boridů, přičemž prvotní testy se zaměřily na možnost boro-karbotermální redukce.

Klíčová slova: karbidy s vysokou entropií, boridy s vysokou entropií, přechodné kovy, karbotermální redukce, vysokoteplotní keramika, metoda sol-gel

Abstract

This master thesis is a follow-up of my bachelor's project, where the goal was to prepare high entropy carbide (HEC), namely (Ti, Zr, Hf, Nb, Ta)C, by the sol-gel method followed by carbothermal reduction using spark plasma sintering facility (SPS). In this work, the first aim is to substitute SPS with ultra-fast high-temperature sintering (UHS) for the same HEC, (Ti, Zr, Hf, Nb, Ta)C. The advantages of UHS compared to SPS are a thousand times lower consumption of electricity and simpler set-up. The second aim is the adaptation of the synthesis for the preparation of HEC of different compositions, (Cr, Mn, Fe, Co, Ni)C. The third aim is the testing of the presented sol-gel technique on the production of borides, while the initial experiments were focused on boro-carbothermal reduction.

Keywords: high entropy carbides, high entropy borides, transition metals, carbothermal reduction, high-temperature ceramics, sol-gel method

Poděkování

Úvodem bych ráda poděkovala Ústavu anorganické chemie AV ČR v.v.i. za poskytnutí skenovacího elektronového mikroskopu pro analýzu vzorků v rámci programu výzkumné infrastruktury NanoEnviCz, podpořeného MŠMT (projekt č. LM2018124).

Dále bych ráda poděkovala MSc. Mariana Gerina a Dr. Danielu Raineru za měření na TEM.

V neposlední řadě bych chtěla poděkovat RNDr. Václavu Tyrpeklovi, Ph.D. a Ing. Petře Ecorchard, Ph.D. za mentorování a přínosné rady.

Contents

List of used symbols and abbreviations

BCC	Body centred cubic
CA	Citric acid
DEMI	Demineralized water
FCC	Face centred cubic
HEAs	High entropy alloys
HEBs	High entropy borides
HECs	High entropy carbides
HEMs	High entropy materials
PDF	Powder diffraction database
PXRD	Powder x-ray diffraction
SEM	Scanning electron microscopy
SPS	Spark plasma sintering
TEM	Transmission electron microscopy
UHS	Ultrafast high-temperature sintering
UHTCs	Ultra-high temperature ceramics

1 Introduction

High entropy materials (HEMs) are broadly used in extreme environments because of their outstanding properties, such as chemical and thermal stability, and excellent mechanical properties. These materials gained their properties thanks to the increase of the configurational entropy by mixing at least five building components (elements) in equimolar ratios. Application of the HEMs is mainly in heavy industry as tools, coatings or reactors. Initial research of HEMs began alongside the development of hypersonic aircraft technology at the end of the 20th century.

The most popular materials that belong to the category of HEMs are carbides, oxides, borides, alloys and nitrates. Each sub-category has some advantages compared to the others. For example, carbides excel with their mechanical durability and borides are mechanically tough and at the same time light in weight.

The general synthesis approach of HEMs lies in conventional metallurgy, such as high-energy ball milling followed by conventional sintering, or usually by Spark plasma sintering (SPS). Because these methods are energetically demanding, less challenging and expensive approaches are in our spotlight. For example, high-energy ball milling can be substituted by the sol-gel technique and SPS by simple and cost-effective Ultrafast high-temperature sintering (UHS).

The UHS's purchase price and operating cost are neglectable compared to SPS's and conventional furnaces. It is because the UHS set-up consists of graphite felt connected to the DC power source in a vacuumable chamber. To imagine, the chamber can be a bigger Erlenmeyer flask or exicator. The SPS device is far more complicated and therefore expensive. In contrary, the UHS apparatus can be set up in every laboratory. One of our goals was to test the UHS system for the preparation of high entropy materials, namely, to conduct the carbothermal reduction of sol-gel derived powders.

2 Theoretical Section

2. 1. Ultra-high temperature ceramics

A new class of resistant ceramics was invented for extremely challenging environments. Ultra-high temperature ceramics (UHTCs) are defined by melting point over 3300 K, which narrows this category to carbides, borides and nitrides of transition metals from IV and V groups. [1]–[3] The strong covalent bond between an anion (carbide, boride or nitride) and a metal cation grants high melting temperatures, hardness and stiffness of the material. [4] Some of the high entropy materials fall into this category.

2. 2. High entropy materials

High entropy materials (HEMs), for example, alloys and oxides, are solid solutions which consist of at least five metal elements with a close atomic radius. Those metal ions are randomly distributed in the lattice which leads to severe distortion. The lattice distortion affects the properties e.g. higher hardness of the materials and lower electrical and thermal conductivity. [5], [6]

High entropy materials can be alloys, carbides, borides, nitrides and oxides of multiple transition metals. [7]–[11] Although these materials contain several transition metals in the lattice, they exhibit a single crystallographic phase. Because of the extraordinary crystal lattice, the mechanical properties of high entropy materials, such as wear, heat and chemical resistance, are enhanced compared to single-element compounds. [12] Thanks to their resistant properties, high entropy ceramics have broad applications in extreme environments, for instance, thermal protection, energy storage, catalysis and even as biocompatible implants. [13]–[16]

The first type of high entropy materials to be mentioned are alloys (HEAs). [17], [18] They consist of at least five metals in an equimolar ratio. Their most important attributes are hardness, mechanical strength, high-temperature resistance and chemical stability, and even oxidation resistance. HEAs are usually prepared by conventional metallurgy processes (alloying). [19]

Another group of materials falling into the high entropy definition are carbides. High entropy carbides (HECs) are widely synthesised via high-energy milling followed by Spark plasma sintering (SPS). For HECs of early-transition metals, e.g. (Ti, Zr, Hf, Nb, Ta)C, high-energy milling can be substituted by the sol-gel method. [20]

2. 3. High entropy alloys

Alloys with high entropy (HEAs) were the first high entropy materials ever developed. HEAs contain again multiple alloying elements compared to conventional alloys. [21]–[23] HEAs are in most cases prepared by classical metallurgy procedures, such as melting, recrystallization and casting. [24] In the ideal case, while cooling down the alloy melts crystallize in single-phase, mostly body (BCC) or face (FCC) centred cubic phase. For example, Cr, Mn, Fe, Co, and Ni, create only FCC phase alloy. For alloys composed of six to eight metals, the BCC phase starts to be predominant. [17] Generally, the phase formation is mainly affected by the enthalpy versus entropy state. [19] Due to their exceptional properties (high chemical, wear, thermal and oxidation resistance) are HEAs used as mould dies, strained mechanical parts and even furnace parts. [25]

The stabilization of HEAs can be caused by one element, which creates a main structure. For example, Itoh et al. [26] describe the stability of alloys with vanadium as the supporting metal. Vanadium creates a BCC structure, and the remaining metals fill in the vacant cavities in the structure. The stability of HEAs can be also affected by the homogeneity of the final material. [26], [27]

2. 4. High entropy borides

High entropy borides (HEBs) belong to UHTCs alongside the carbides and nitrides of early-transition metals. Five-component borides have typically a hexagonal structure, similar to mono-metal diborides, such as AlB_2. They have a sandwich-like structure (see Figure 1), where 2D layers of metallic cations (orange) and boron anion (blue) are altered. [28], [29]

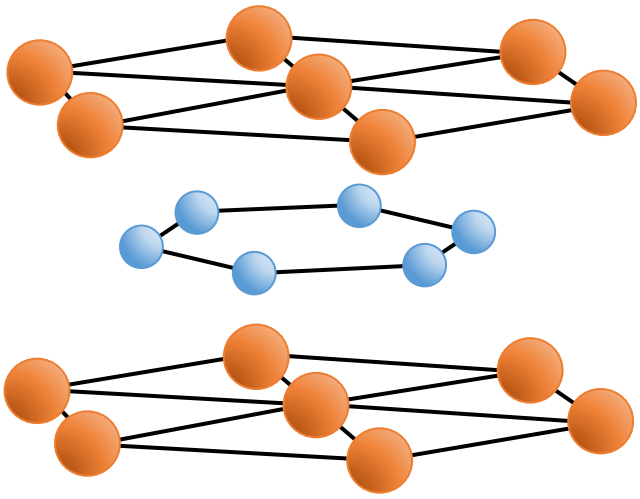

Figure 1 - Structure of AlB_2.

Both present bonds, the covalent bond between B–B and the ionic-covalent bond between metal and boron, play an important role in HEBs' stability. [30] The main properties of HEBs are their hardness and oxidation resistance even at elevated temperatures. [29] Although, the hardness of some borides, as with Ti, Zr and Hf, decreases with increasing temperature. [31] The thermal conductivity of diborides is almost five times higher than carbides or nitrides. [4]

2. 4. 1. Synthesis of HEBs

Common synthesis of multi-metal HEBs is high-energy milling of individual metal-diborides followed by annealing with spark plasma sintering (SPS). [28] To prepare single-phase HEBs by SPS, the annealing temperature should not exceed over 1200 K. When the temperature exceeds 1400 K, additional phases begin to show in PXRD diagrams. Usually, these phases are also borides, but they do not include all initial metals. [29], [32]

Individual metal-diborides can be substituted with metal-oxides and carbon precursors leading to boro-carbothermal reduction. [30] SPS can be replaced by annealing with a microwave-induced plasma furnace. At 1780 K for 45 minutes precursors are fully converted to single-phase HEB. [33] Oxygen impurities are a significant problem during densification. The presence of oxygen leads to the loss of boron in the form of B_2O_3, which sublimate around 1770 K. To reduce the problem, B_4C is added to the precursors. [34]

2. 5. High entropy carbides

High entropy carbides (HECs) crystallize typically in cubic phase with rock salt (NaCl) structure ($Fm\bar{3}m$) depicted in Figure 2, where cations of metals are orange and anions of carbide are blue. This type of structure tolerates existence of carbon vacancies in octahedral cavities of metal sublattice. This can lead to non-stoichiometric compounds. [35]

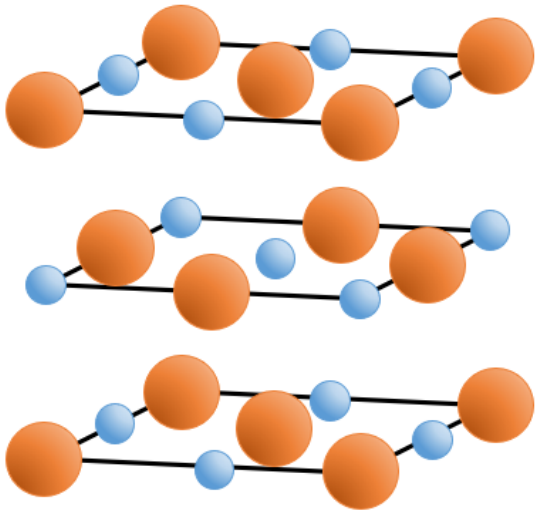

Figure 2 - Structure of HECs.

As mentioned earlier, HECs contain multiple metal ions with similar atomic radius in a cubic carbide lattice. A properly chosen combination of those metals improves desired mechanical properties of carbide. [36], [37] For example, polymetallic HEC (Ti, Zr, Hf, Nb, Ta)C exceeded twice the mechanical resistance of individual carbides. [38], [39] On the other side, the heat resistance decreases due to the metal mixing. For instance, HfC has a melting point at 4200 K and TaC has 4100 K, however, HfTaC has a melting point at 4040 K. [40], [41]

Thanks to their exceptional mechanical properties, HECs are used as drill bits, cutting tools and even as thermal protection coating on hypersonic aircraft. [42], [43] Among mechanical properties, HEC, particularly (Ti, Zr, Nb, Hf, Ta)C, is used as a coating material for metallic biomedical implants. [16]

2. 5. 1. Synthesis of HECs

Typically, HECs are prepared by powder metallurgy techniques followed by sintering by SPS. Precursors are either carbides of individual metals [44], [45] or elementary metals and a source of carbon [35]. Those precursors undergo high-energy milling for tens of hours. Another synthesis is the carbothermal reduction of metal oxides in an inert atmosphere. [46], [47] Final carbide is later treated at high temperature for better homogeneity.

Additionally, carbides can be prepared from metal oxide/active carbon composites obtained by sol-gel synthesis. For example, Salvato et al. [48] used the sol-gel method for the preparation of UC. As precursors, they use uranyl nitrate as a metal precursor and citric acid as a carbon precursor. This synthetic route was based on the work of Matović et al. [49], who came up with the idea to prepare HfC by sol-gel method in water as a solvent. They used hafnium chloride as a metal precursor. In my bachelor's thesis, we adapted this water-based sol-gel method for the preparation of (Ti, Zr, Hf, Nb, Ta)C, one of the most typical HEC. [20]

2. 6. Spark plasma sintering

Spark plasma sintering (SPS) is a sintering/compaction method which belongs to the electrical field/current-assisted sintering techniques. Nowadays, it is also broadly used for the synthesis of high-entropy ceramics. [50], [51] Sample is uniaxially pressed by graphite punches (see Figure 3). Certain electrical power (up to tens of kW) is applied on the set-up through typically set voltage and varying currents. For conductive samples, the current passes through the specimen. For non-conductive samples, the current passes through the graphite die and punches around the sample. In both cases, the resistance of graphite generates heat through Joule heating. [52]

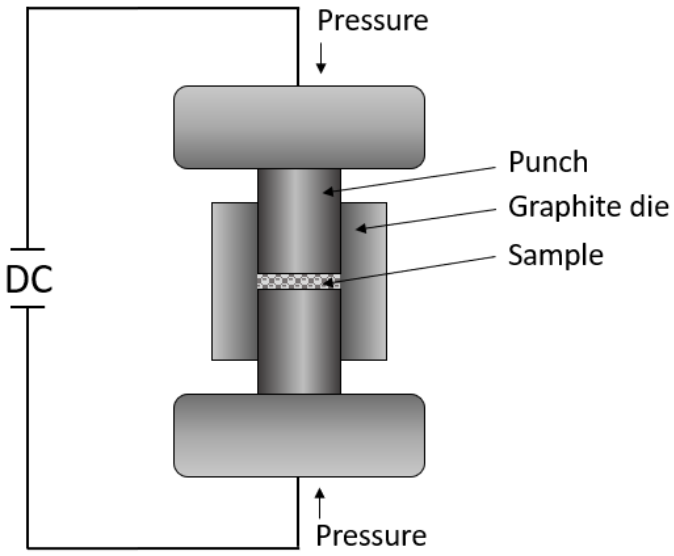

Figure 3 – Schema of spark plasma sintering apparatus.

Materials obtained by SPS have usually smaller grain sizes and have a higher density at milder conditions than conventionally sintered. [53], [54] Not only have materials synthesised in SPS better properties, but this method has lower energy consumption compared to other conventional compacting/sintering methods, such as hot-pressing. Typically, the energy consumption is from units to tens of kWh per calcination cycle. Concerning SPS, the heat is generated in the pressing tools, whereas hot-pressing needs an external heat source, for instance, an induction coil furnace. [54]–[56] When calcining in conventional furnaces the consumption is typically tens of kWh per calcination cycle. For the synthesis of refractory materials, energy consumption presents a significant factor in the price of products.

2. 7. Ultrafast high-temperature sintering

Annealing or sintering of materials can be done using the ultrafast high-temperature sintering [57], which is described in this thesis.

In a recent study, Wang et al. [58] developed ultrafast high-temperature sintering (UHS). This method is based on annealing with Joule heat. The apparatus for UHS consists of the graphite felt anchored between two holders attached to a DC power source (see Figure 4). The sample is put inside the graphite felt in which the DC power is dissipated. The combination of the small weight and low thermal capacity of the felt causes all the energy to be transferred to heat (radiation) [59]. The main advantages of UHS are a fast-heating rate, low energy consumption and simple set-up. The sample is heated by flowing current through the carbon felt in the inert atmosphere. Depending on the type of set-up, the temperature can climb up to 3000 °C.

The results from our laboratory recently showed that a high-density pellet of refractory oxide (gadolinium doped ceria) can be produced using UHS with an energy consumption of less than 20 W/h per calcination cycle. [60] Also, the final sample can be almost any desired shape, not only in a form of a pellet. [61] The heating rate can reach 10^4 K/min, which keeps a high densification rate by eliminating initial grain coarsening.[62], [63] Similarly to SPS, UHS can be used for densification/sintering and synthesis. [64], [65]

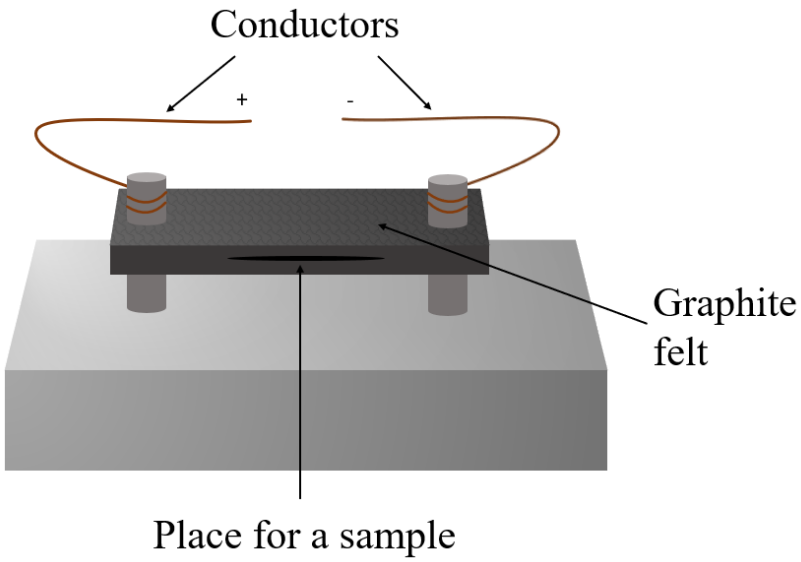

Figure 4 - Schema of UHS apparatus.

3 Experimental Section

The thesis can be divided into the following parts:

- The UHS set-up construction, adjustment, and calibration.
- The sol-gel preparation of (Ti, Zr, Hf, Nb, Ta)C and adaptation for a carbothermal reduction in the UHS apparatus.
- Testing of new HEC composition, namely (Cr, Mn, Fe, Co, Ni)C, to extend the preparation technique on new compositions.
- Finally, checking the possibility of boro-carbothermal reduction in UHS with the aim of future HEB synthesis.

3. 1. Used chemicals

All chemicals (see Table 1) were used as were without further purification.

Table 1 - Used chemicals.

Substance	Purity	Concentration	Supplier
$ZrOCl_2$ in HCl	-	30 %	Sigma – Aldrich
$TiCl_3$ in HCl	-	≥ 12 %	Sigma – Aldrich
$NbCl_5$	99 %	-	Alfa Aesar
$TaCl_5$	99.8 %	-	Alfa Aesar
$HfCl_4$	98 %	-	Sigma – Aldrich
Citric acid	99.8 %	-	VWR Chemicals
H_2O_2	-	33 %	VWR Chemicals
NH_4OH	-	25 %	Lach – Ner
H_3BO_3	99.8 %	-	Roth
$CoCl_2 \cdot 6H_2O$	> 99 %	-	Lach-Ner
$CrCl_3 \cdot 6H_2O$	> 98 %	-	Lach – Ner
$FeCl_3 \cdot 6H_2O$	98 %	-	HiChem
$NiCl_2 \cdot 6H_2O$	> 98 %	-	Penta
$MnCl_2 \cdot 4H_2O$	> 99 %	-	Sigma – Aldrich

3. 2. Synthesis approach

3. 2. 1. Calibration of UHS

The temperature measurement in UHS presents a technological challenge. With heating rates of 10^4 K/min, the measurements are done by thermocouples or pyrometers with significant complications. This is bypassed by an internal standard, so the calibration of the system temperature was done by melting chosen substances concerning applied current/power conditions. Those were MoO_3, copper, nickel and platinum metals. Their melting points are in Table 2. The voltage/current combinations with increasing total power were applied to the system for 60 seconds (typical calcination cycle) and the melting of standards was tracked. The total power dissipated in the graphite felts was adjusted by the voltage/current settings of the DC source. The temperature of the felts obviously increases with the applied power.

Table 2 - Melting points of tested substances.

	MoO_3	Cu	Ni	Pt
Melting temperature [°C]	795	1085	1455	1750

3. 2. 2. Synthesis of (Ti, Zr, Hf, Nb, Ta)C

The synthesis of (Ti, Zr, Hf, Nb, Ta)C is based on the one developed in my bachelor's thesis. [20] Chlorides were used as metal precursors, respectively chloride-oxide of Zr, and citric acid (CA) as carbon precursor. All precursors, except for $TaCl_5$, were dissolved in H_2O_2 with part of CA. $TaCl_5$ was dissolved in a separate beaker with the rest of CA and ammonia solution. The pH needs to be circa 10 to create peroxocitrato-complex which is soluble in an aqueous solution. The homogenous solution was heated to 80 °C and thickened to a gel in a rotary evaporator. The gel was pyrolyzed in a modified tube furnace in an argon atmosphere at 800 °C with no dwell. The heating rate was 5 °C/min. The pyrolyzed intermediate was annealed in UHS to perform the carbothermal reduction under different power and time conditions. In summary, the synthesis was done by the so-gel method followed by high-temperature firing. In the past, we conducted the carbothermal reduction in a modified SPS. The presented work aimed to adjust the reaction set up to UHS. The whole synthesis is depicted in Figure 5.

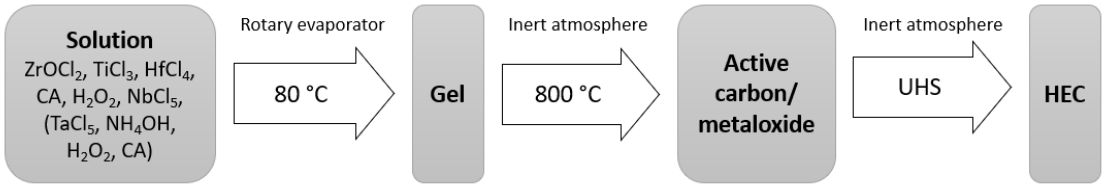

Figure 5 - Diagram of synthesis approach of (Ti, Zr, Hf, Nb, Ta)C.

3. 2. 3. Synthesis of (Cr, Mn, Fe, Co, Ni)C

Similarly, as described above, the preparation route was used for a new composition - (Cr, Mn, Fe, Co, Ni)C. All metal precursors, chlorides, and carbon precursor (CA) were dissolved in demineralized (DEMI) water. The homogenous solution was concentrated into a gel by a vacuum rotary evaporator. The gel was pyrolyzed in argon at 800 °C without dwell and a heating rate of 5 °C/minute. The carbothermal reduction was done in the UHS apparatus. The whole synthesis is summarized in Figure 6.

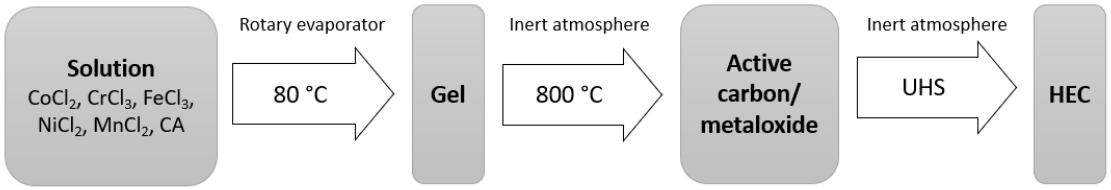

Figure 6 - Diagram of synthesis approach of (Cr, Mn, Fe, Co, Ni)C.

3. 2. 4. Boro-carbothermal reduction

The synthetic route was tested for the possibility of boride preparation. As a first step, the boro-carbothermal reduction was followed, done in a similar way to previous experiments on HEC materials. The boric acid was dissolved in DEMI water at 80 – 90 °C, then CA was added in different molar ratios, and pH was adjusted to 8, respectively 11, with an ammonia solution. The homogenous solution was evaporated into the gel. The gel was pyrolyzed in an argon atmosphere at 600 °C with no dwell and a heating rate of 5 °C/minute. An amorphous substance was annealed in UHS to study the reaction, which would lead primarily to boron carbide (B_4C). An overview of synthesis is in Figure 7.

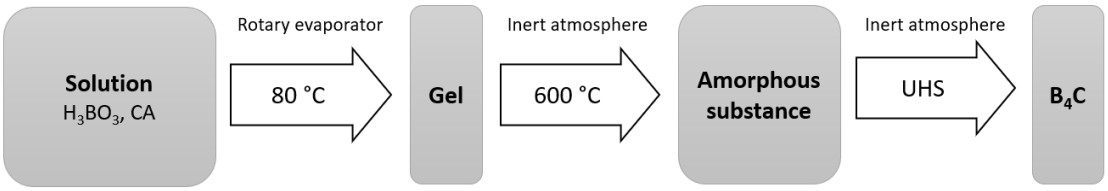

Figure 7 - Diagram of synthesis approach of B_4C.

3. 3. Calcination in an inert atmosphere and UHS

Tube furnace was used for the pyrolysis under inert conditions. A tube made of quartz glass was put inside the furnace and was connected to a vacuum/inert line (see Figure 8). A balloon was availed for better control of argon over-pressure inside the apparatus.

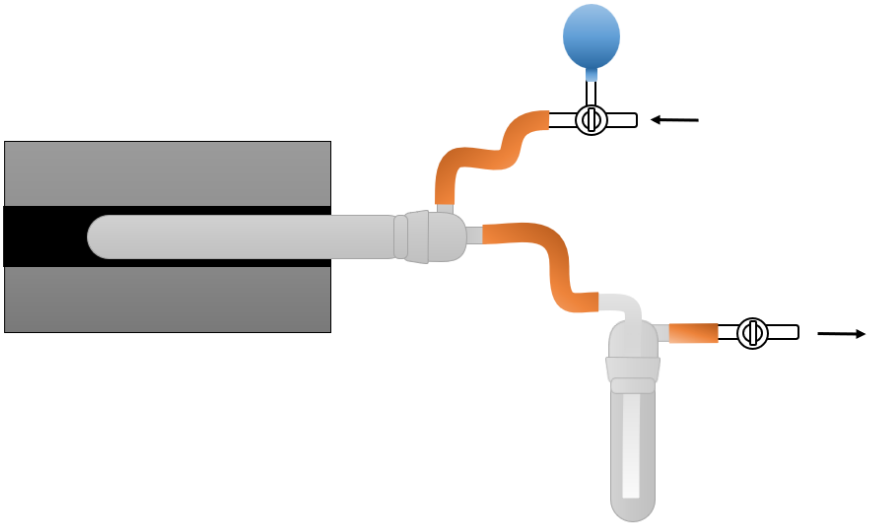

Figure 8 - Adapted tube furnace. Arrows show the flow of argon in and out.

For annealing, the apparatus for UHS was used (see Figure 9). The graphite felt was placed in a modified exicator. Acetate silicone is suitable for higher temperatures and was applied between the upper and lower pieces of the exicator. Tubes for argon flow and wires were put through the silicone. With this set-up, annealing in an inert atmosphere is possible. Also, thick borosilicate glass of exicator withstands higher temperatures.

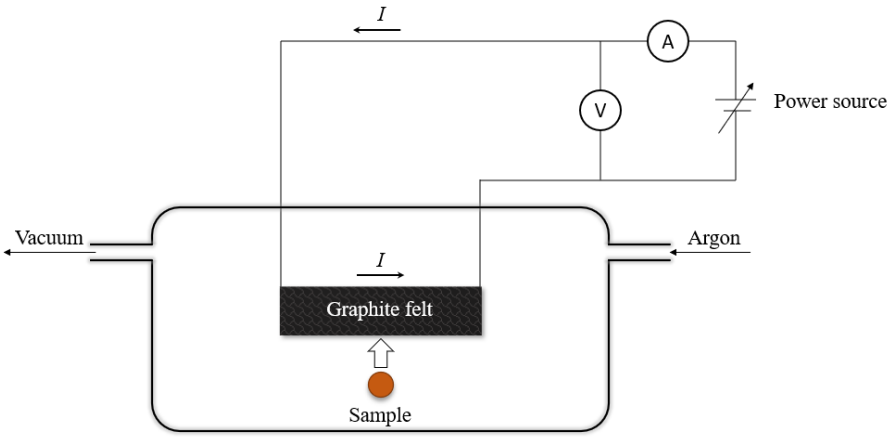

Figure 9 - Diagram of apparatus for UHS with DC source.

3. 4. Analytical techniques and instruments

3. 4. 1. DC power supply

For UHS as a DC power supply PSW 30-72 with a maximum performance of 720 W by GW INSTEK was used.

3. 4. 2. Powder X-Ray diffraction (PXRD)

Samples were measured with PANalytical X´pert PRO with a secondary monochromator (Cu K_α λ = 1.5418 Å) and PIXcel detector. The Faculty of Sciences, Charles University in Prague provided the instrument.

Samples were measured from 5° to 90° of 2θ with 0.0262606 ° step and 150.45 s per step and total measuring time 33 minutes.

3. 4. 3. Scanning electron microscopy (SEM)

SEM has been done FEI Nova NanoSEM microscope. The instrument was provided by the Institute of Inorganic Chemistry of the Czech Academy of Sciences in Řež. The samples were deposited on a silicon chip or adhesive carbon slice.

3. 4. 4. Transmission electron microscopy (TEM)

TEM has been measured on JEOL JEM-NEOARM 200F with a working voltage of 30 – 200 kV and CMOS camera (4096 x 4096 pixels, up to 200 fps redout).

The samples were grinded in mortar and powdered on a carbon coated Cu grid.

3. 5. Prepared samples

Table 3 is an overview of selected samples concerning the preparation of (Ti, Zr, Hf, Nb, Ta)C. The sample with a molar ratio of all metals and citric acid (M:CA) = 0.9:1 was prepared in two batches.

Table 3 - All prepared samples of HEC with Ti, Zr, Hf, Nb and Ta.

Sample	Molar ratio of M:CA	Preparation details
MC08-1_800C	0.8:1	Homogenous gel pyrolyzed at 800 °C.
MC08-1_20A	0.8:1	UHS: 20 A, 60 s, 17.5 V
MC09-1_800C	0.9:1	Homogenous gel pyrolyzed at 800 °C.
MC09-1_2-800C	0.9:1	Homogenous gel pyrolyzed at 800 °C.
MC09-1_20A	0.9:1	UHS: 20 A, 60 s, 18.5 V
MC09-1_20A-120s	0.9:1	UHS: 20 A, 120 s, 21 V
MC09-1_22A	0.9:1	UHS: 22 A, 60 s, 15.6 V
MC09-1_22A-120s	0.9:1	UHS: 22 A, 120 s, 17.4 V
MC09-1_22A-300s	0.9:1	UHS: 22 A, 300 s, 14 V
MC11_800C	1:1	Homogenous gel pyrolyzed at 800 °C.
MC11_20A	1:1	UHS: 20 A, 60 s, 19.3 V

All prepared samples during the modification of the synthesis of (Cr, Mn, Fe, Co, Ni)C are listed in Table 4. Samples annealed with a higher set current than 13 A were difficult to process due to electrical sparks.

Table 4 - Prepared samples during synthesis of (Cr, Mn, Fe, Co, Ni)C.

Sample	Molar ratio of M:CA	Preparation details
cm08-1_800C	0.8:1	Homogenous gel pyrolyzed at 800 °C.
cm08-1_20A	0.8:1	UHS: 20 A, 60 s, 16 V
cm09-1_800C	0.9:1	Homogenous gel pyrolyzed at 800 °C.
cm11_800C	1:1	Homogenous gel pyrolyzed at 800 °C.
cm11_2-800C	1:1	Homogenous gel pyrolyzed at 800 °C.
cm11_13A-300s	1:1	UHS: 13 A, 300 s, 10.5 V
cm11_2-13A-300s	1:1	UHS: 13 A, 300 s, 12.5 V
cm11_2-13A-600s	1:1	UHS: 13 A, 600 s, 13.1 V
cm11_2-13A-900s	1:1	UHS: 13 A, 900 s, 11.7 V
cm11_2-15A-600s	1:1	UHS: 15 A, 600 s, 10.6 V

For simplification, Table 5 shows only annealed samples in UHS and modified tube furnace. All listed samples were pH adjusted to 8 before they were concentrated in a gel. The pyrolyzed gels at 800 °C and 600 °C are not listed.

Table 5 - Annealed samples with pH adjustment to pH 8 during synthesis of B_4C.

Sample	Molar ratio of M:CA	Preparation details
cb04-1_1000C	0.4:1	Tube furnace in inert atmosphere at 1000 °C
cb05-1_20A	0.5:1	UHS: 20 A, 60 s, 15.5 V
cb05-1_1000C	0.5:1	Tube furnace in inert atmosphere at 1000 °C
cb06-1_13A	0.6:1	UHS: 13 A, 60 s, 13 V
cb06-1_15A	0.6:1	UHS: 15 A, 60 s, 14.5 V
cb06-1_15A-300s	0.6:1	UHS: 15 A, 300 s, 12.5 V
cb06-1_15A-600s	0.6:1	UHS: 15 A, 600 s, 14 V
cb06-1_17A	0.6:1	UHS: 17 A, 60 s, 14 V
cb08-1_1000C	0.8:1	Tube furnace in inert atmosphere at 1000 °C
cb08-1_20A	0.8:1	UHS: 20 A, 60 s, 15 V
cb11_22A-300s	1:1	UHS: 22 A, 300 s, 13.5 V
cb11_20A	1:1	UHS: 20 A, 60 s, 15.5 V
cb12-1_20A	1.2:1	UHS: 20 A, 60 s, 15 V
cb15-1_20A	1.5:1	UHS: 20 A, 60 s, 16 V
cb21_20A	2:1	UHS: 20 A, 60 s, 15 V

4 Results and Discussion

4. 1. UHS testing and calibration

After the construction of the UHS apparatus, the calibration of temperature was needed. The applied current and measured voltage are summed up in Table 6. Estimated temperatures were matched with the melting points of tested substances, those are listed in Table 2.

Table 6 - Calibration table of temperatures.

$T_{estim.}$ [°C]	I_{SET} [A]	MoO_3	Cu	Ni	Pt
	5	x (7.4 V)	x	x	x
	7	x (9.3 V)	x	x	x
	7.5	x (11.4 V)	x	x	x
	8	x (12.4 V)	x	x	x
± 800	8.5	Melted (11.4 V)	x	x	x
	10		x (13 V)	x	x
	12		x (12.4 V)	x	x
± 1100	13.5		Melted (12.1 V)	x	x
	15			x (17.4 V)	x
	16			x (14.7 V)	x
± 1500	17			Melted (17.8 V)	x
	17.5				x (14 V)
	20				x (18 V)
± 1800	22				Melted (29 V)

The heat dissipation in graphite felt was captured by the infrared camera Flier TG297 (see Figure 10). Temperature grows with higher current. The graphite felt was the hottest in the middle and its edge was gradually cooling. The temperature reading from the central spot of the camera are only indicative and do not represent the actual temperature in the sample area.

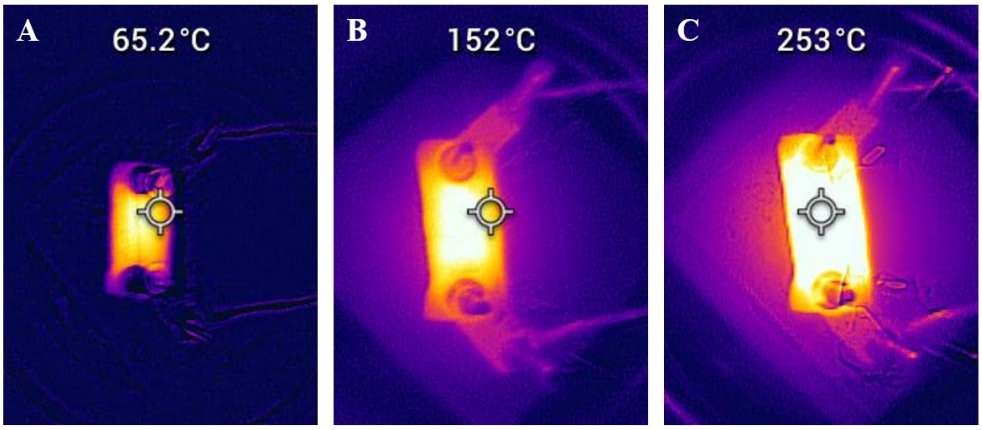

Figure 10 - Heat dissipation of graphite felt at different set currents: A) 5 A, B) 10 A, and C) 15 A.

4. 2. Synthesis of (Ti, Zr, Hf, Nb, Ta)C

Powder diffractograms of pyrolyzed samples at 800 °C with molar ratios of all metals to citric acid (M:CA) equal to 0.8:1, 0.9:1 and 1:1 are in Figure 11. The broad peak at 30° of 2θ belongs to amorphous carbon from pyrolyzed citric acid. More recognisable peaks come from oxides of present metals (Ti, Zr, Hf, Nb and Ta). The oxides are difficult to distinguish because of their mixed structure of the solid solutions. The crystallisation of the mixed oxide is more significant for lower amounts of citric acid (less active carbon). For higher content of citric acid, the sample remains fully amorphous.

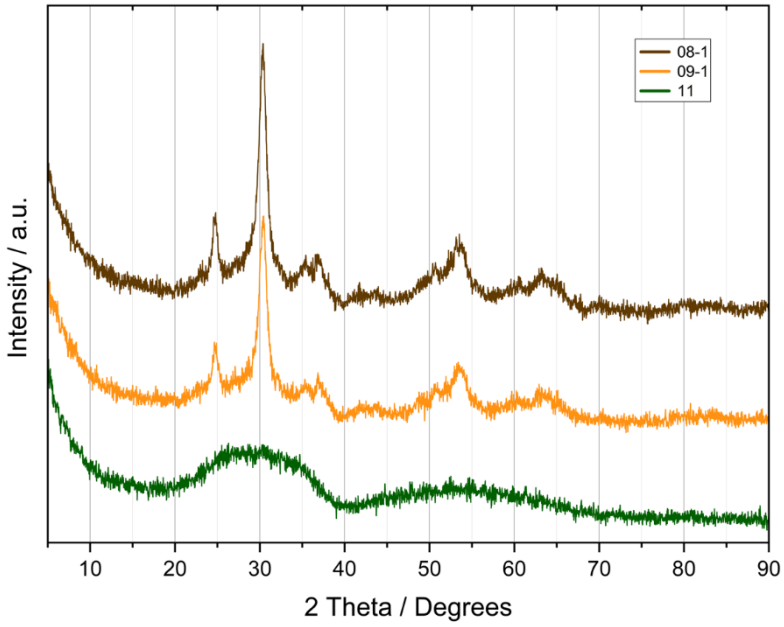

Figure 11 - Powder X-Ray diffractograms of pyrolyzed samples at 800 °C with molar ratio Metals:CA = 0.8:1 (brown), 0.9:1 (yellow), and 1:1 (green).

SEM photos of the pyrolyzed sample at 800 °C with a molar ratio M:CA = 0.9:1 are shown in Figure 12. The left picture (A) shows the various morphology of the sample. In the right picture (B) detailed focus on the porosity of the sample can be seen, which is typical for active carbon from pyrolyzed citric acid.

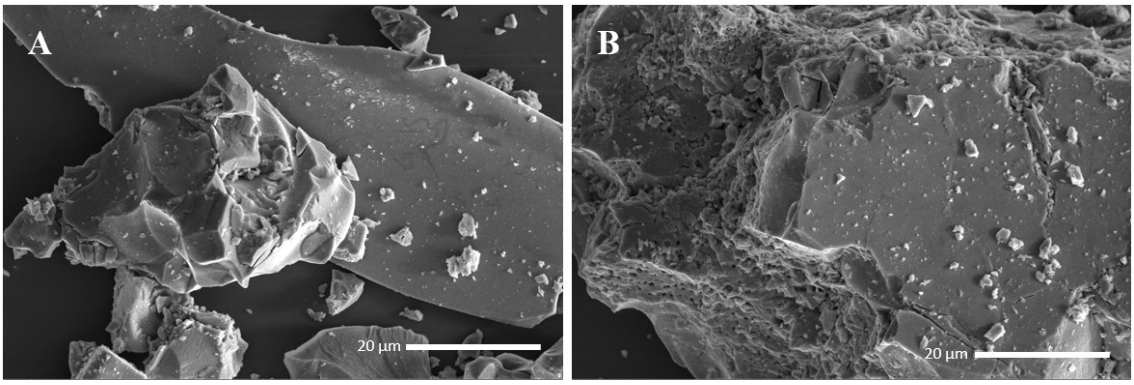

Figure 12 - SEM of a pyrolyzed sample at 800 °C with molar ratio M:CA = 0.9:1.

The samples described above were annealed in a UHS set-up with a set current of 20 A for 60 s. Powder diffractograms of annealed samples are in Figure 13. The peaks of metal oxides (marked with a blue dot) disappear with higher content of carbon.

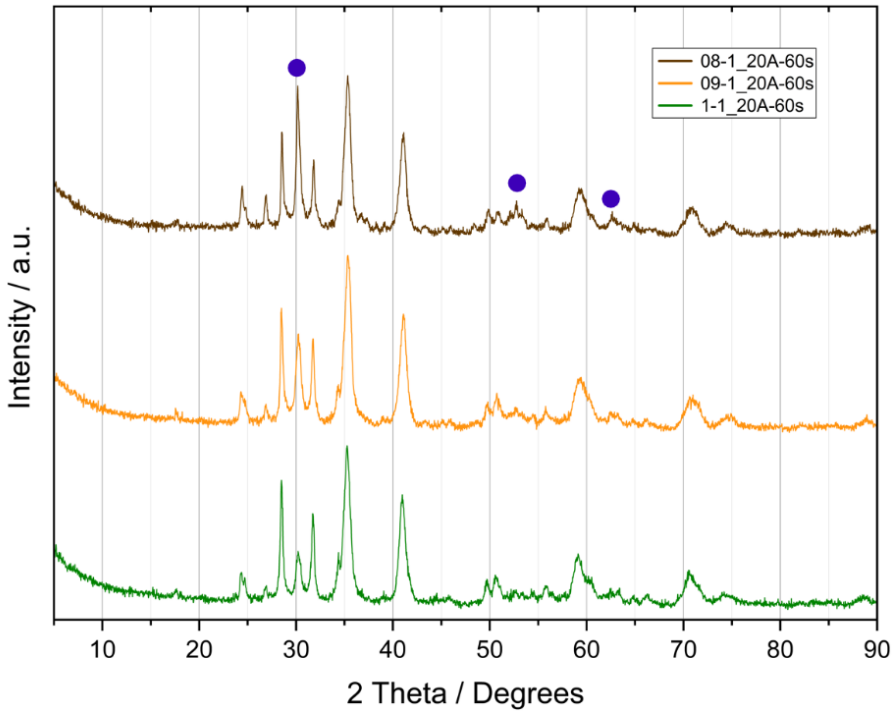

Figure 13 - Powder diffractograms of samples annealed by UHS with set current 20 A for 60 s. Peaks from metal oxides are marked with blue dots.

In Figure 14, there are powder diffractograms of the samples with molar ratio M:CA = 0.9:1 annealed in a UHS set-up with two different set currents and various annealing times. The most intensive peak of metal oxide (at 30° of 2θ) vanishes with three aspects: with longer time at the same temperature, with higher temperature and with higher carbon content. The disappearance of the metal oxide peaks is caused by the higher conversion to carbide through the carbothermal reaction. The HEC of Ti, Zr, Hf, Nb and Ta was obtained with a set current of 22 A and 300 s dwell. The reference is HEC of the same metals prepared with SPS in my bachelor's thesis. [20] According to the powder diffractogram, the prepared HEC is not in one phase, although the main phase is the dominant one. Further research needs to be done.

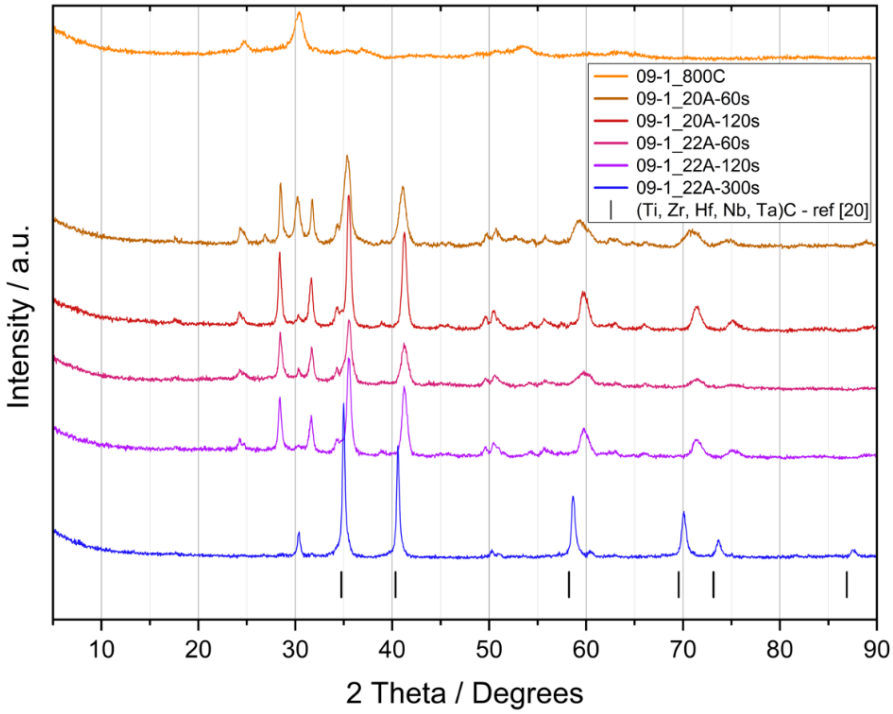

Figure 14 - Powder diffractograms of the sample with molar ratio metals:CA is 0.9:1 with different set currents and annealing times.

Figure 15 shows pictures from SEM of annealed (22 A, 300 s) sample of HEC (Ti, Zr, Hf, Nb, Ta)C with molar ratio M:CA = 0.9:1. In the left picture (A) is the characteristic porosity of the HEC sample. In the right picture (B) second phase, according to powder diffractograms probably metal oxide, can be seen (small particles marked with red arrows). In the bottom picture (C) there is a contamination with graphite felt fibres, in which were samples annealed. The circa 15 μm long fibre is marked with a red arrow.

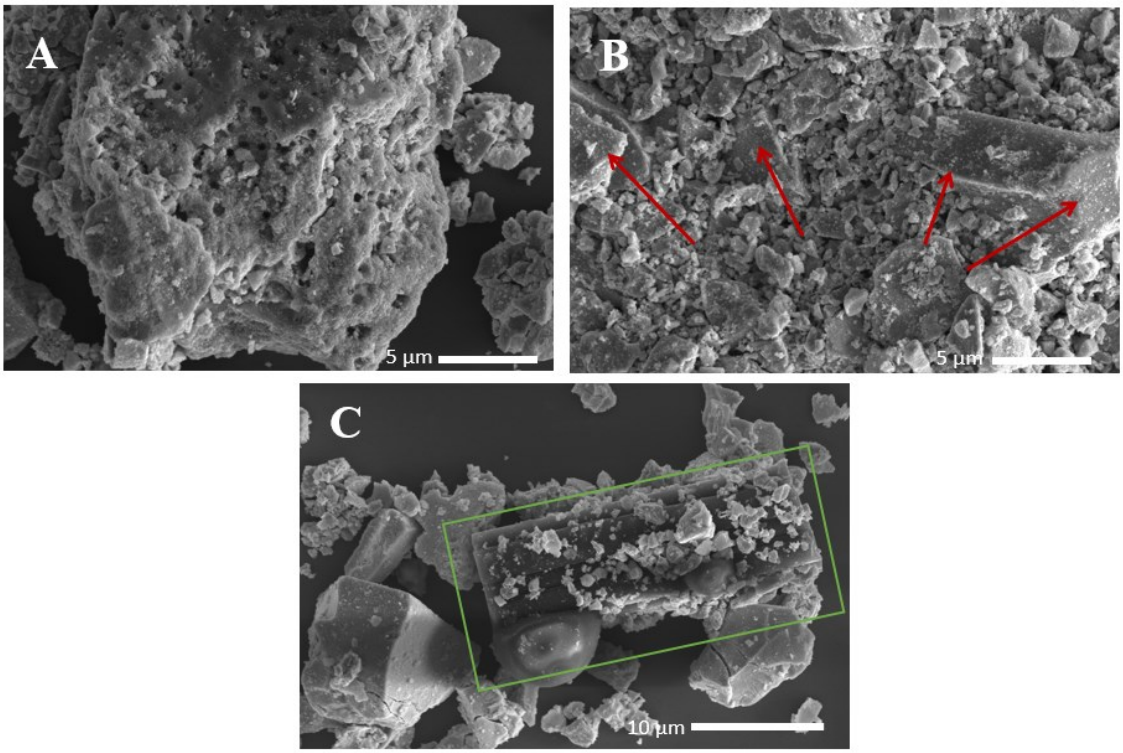

Figure 15 - Pictures from SEM of (Ti, Zr, Hf, Nb, Ta)C annealed with current set at 22 A for 300 s. The red arrows in the picture B shows at particles of another phase. In the picture C green square shows the fibre from graphite felt.

4. 3. Synthesis of (Cr, Mn, Fe, Co, Ni)C

In Figure 16, there are powder diffractograms of (Cr, Mn, Fe, Co, Ni)-C with a molar ratio of all metals to citric acid (M:CA) equal to 1:1. Longer dwell at 13 A leads to a higher conversion rate of carbothermal reduction. Peaks of the FCC phase of the alloy are marked with red dots and the reference is from [66]. In general, sample treated at 800 °C in inert atmosphere contains mixture of HEA and HEO of the elements, as can be seen in diffraction pattern in Figure 16. [67] The UHS treatment then converts the remaining oxide to HEA and with increased time the carbide peaks start to appear.

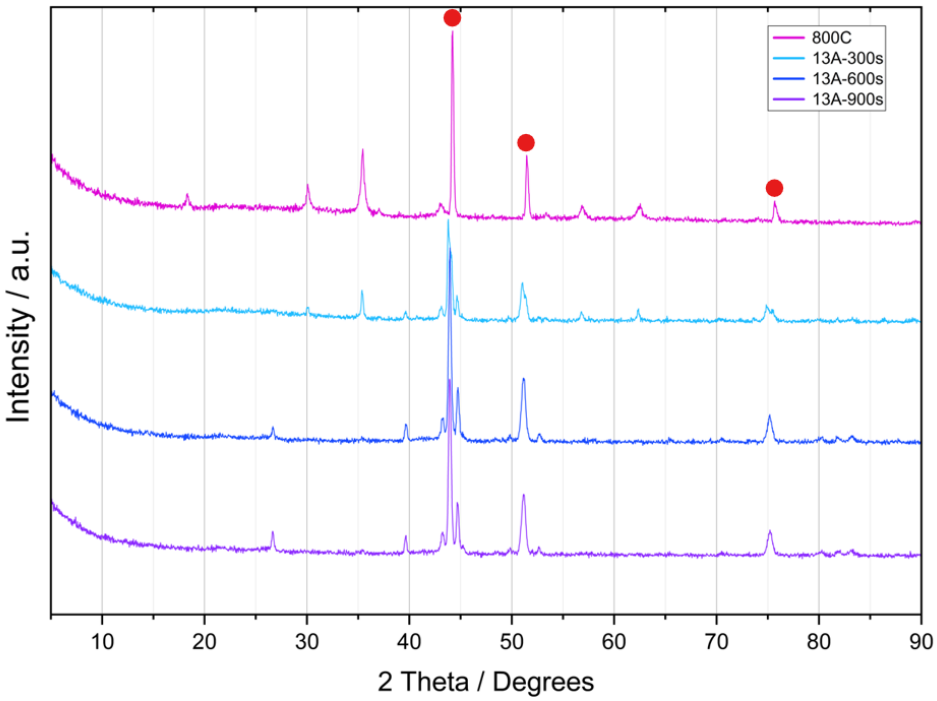

Figure 16 - Powder X-Ray diffractograms of (Cr, Mn, Fe, Co, Ni)C: pyrolyzed at 800 °C (pink) and annealed with set current at 13 A for 300 s (light blue), for 600 s (dark blue), and for 900 s (purple). Red dots mark peaks from FCC phase of alloy. [66]

Figure 17 presents powder diffractograms of samples annealed in UHS with 13 A for 900 s with three different molar ratios, namely C:M equal 1:1, 1.5:1 and 2:1. With this increased carbon content, enough material should be present for the carbothermal reduction. Peaks of HEA are marked with blue dots. [66]

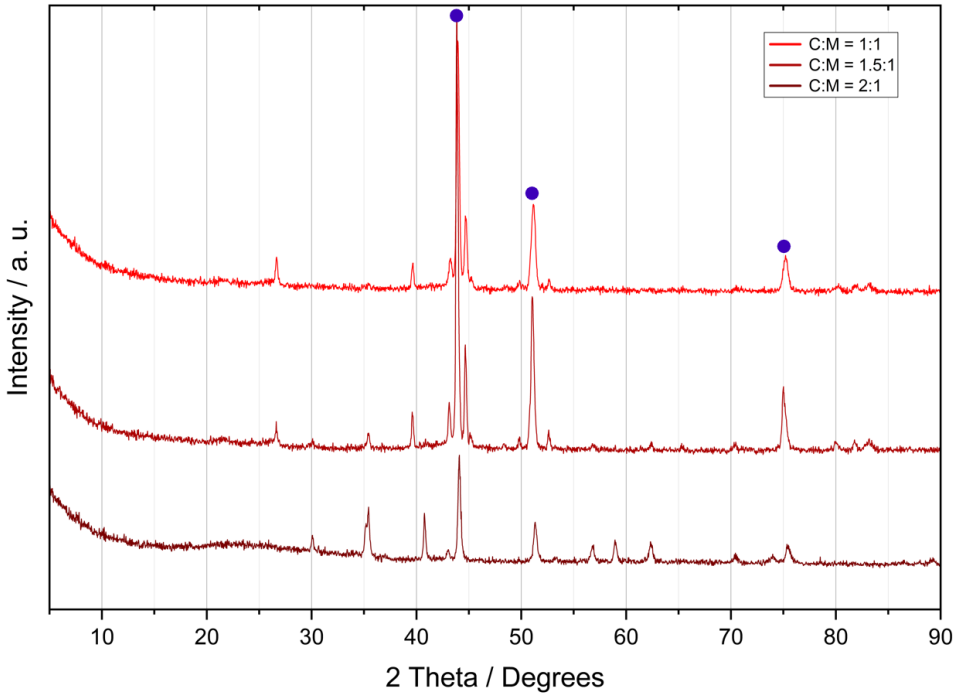

Figure 17 - Powder diffractograms of HEC with Cr, Mn, Fe, Co, Ni with molar ratios of CA to all metals equal to 1:1, 1.5:1, and 2:1 annealed with UHS with set current 13 A for 900 s. Blue dots mark peaks from HEA. [66]

Apart from HEA diffraction lines the other reflections are difficult to assign to specific compounds, since the Powder Difraction Database (PDF) is not rich in carbide compounds of such type. However, following data treatment was performed – the reflections wer compared with single metal carbides of used metals. For example, iron forms cementite Fe_3C upon reduction, manganese and nickle should similarly form Mn_3C and Ni_3C. Chromium forms several carbides Cr_3C_2, Cr_7C_3, and $Cr_{23}C_6$. And finaly cobalt forms typically Co_2C. Appart from the HEA pattern, the sample with highest carbon conent (ratio 2:1) shows no other predominant phase know in the PDF database. The diffraction pattern was compared with PDF cards of single carbides, namly, $Mn_{23}C_6$ (00-028-0646), Fe_2C (00-017-0897), Fe_3C – cementite (00-034-0001) and Co_2C (00-050-1371). Unfortunately, no clear pattern match was identified and most probably multiple ellements form a carbide of unkown composition and pattern.

SEM measurements of the pyrolyzed sample at 800 °C and annealed sample with 13 A for 900 s are in Figure 18. The morphology of pyrolyzed sample is in picture Figure 18A. The sample shows characteristic bubbles formed due to the gas release from pyrolyzed CA (red arrow), droplets of alloy (green arrows) and particles of metal oxides (yellow

arrow) are observed. Photos of the overview morphology of the annealed sample are in Figure 18B and C. Close up in Figure 18D. The globules of alloy in Figure 18C are bigger than in Figure 18A. This can be explained by the temperature used for annealing being around the melting points of the present metals. In Figure 18D, the particles are trapped in the active carbon. The annealed sample with UHS is unfortunatelly contaminated with fibres from griphite felt (Figure 18B – blue arrows).

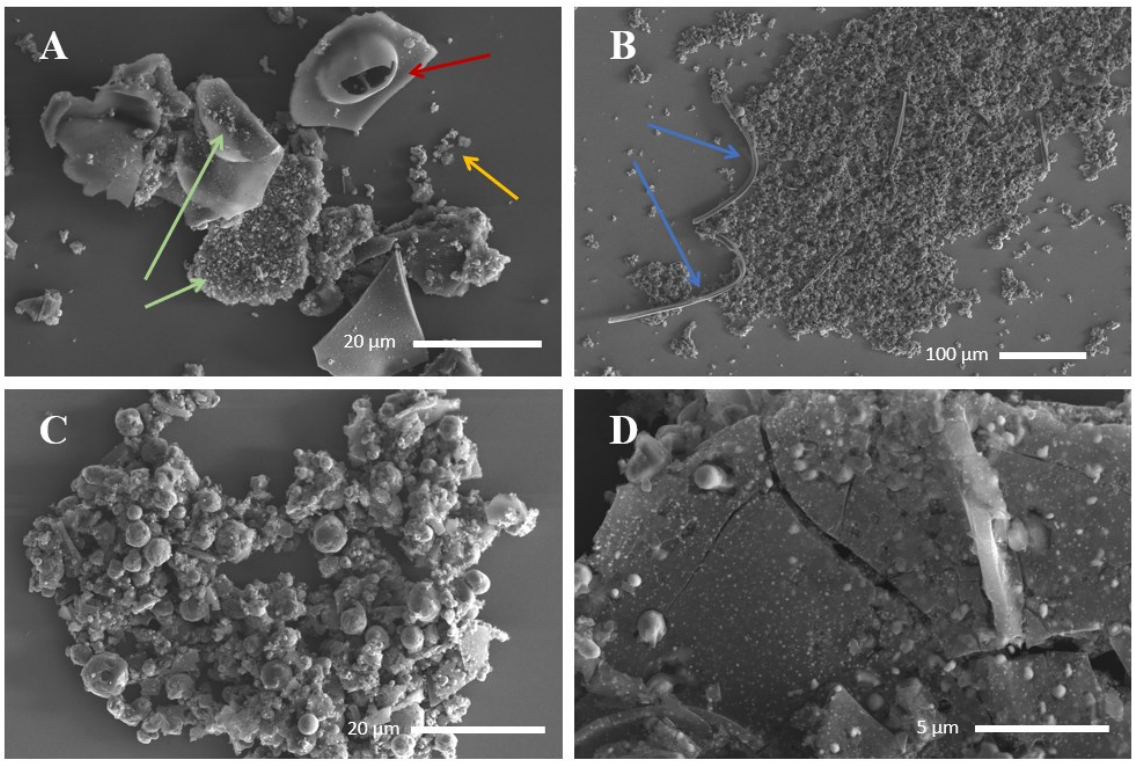

Figure 18 - SEM photos of (Cr, Mn, Fe, Co, Ni)C with molar ratio M:CA = 1:1: pyrolyzed at 800 °C (A) and annealed by UHS with 13 A for 900 s overall morphology (B,C) and close up (D).

TEM measurements of (Cr, Mn, Fe, Co, Ni)C with molar ratio M:CA = 1:1 pyrolyzed at 800 °C are in Figure 19. Nanoparticles of metal oxides are embedded in the matrix of amorphous carbon. Such a high-phase interface obtained by the sol-gel synthetic route would be hardly achievable by common metallurgic methods.

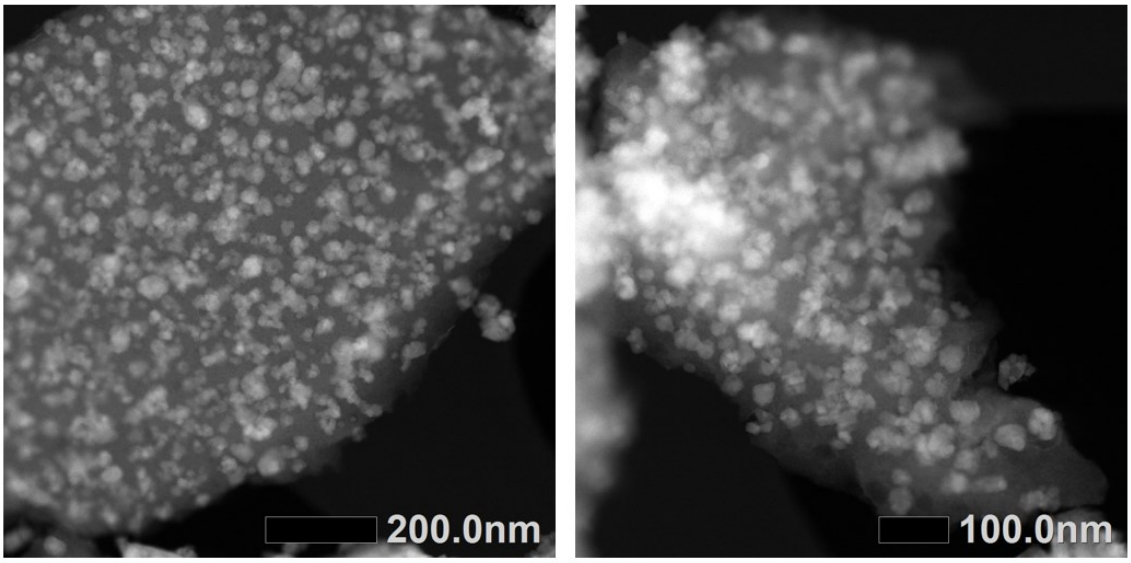

Figure 19 - TEM photos of (Cr, Mn, Fe, Co, Ni)C with molar ratio M:CA = 1:1 pyrolyzed at 800 °C.

For comparison, annealing in a tube furnace in an inert atmosphere at 1000 °C was done. Powder diffractograms of these samples are shown in Figure 20. The temperature was low for the carbothermal reduction. Peaks of HEA are marked with blue dots. [66]

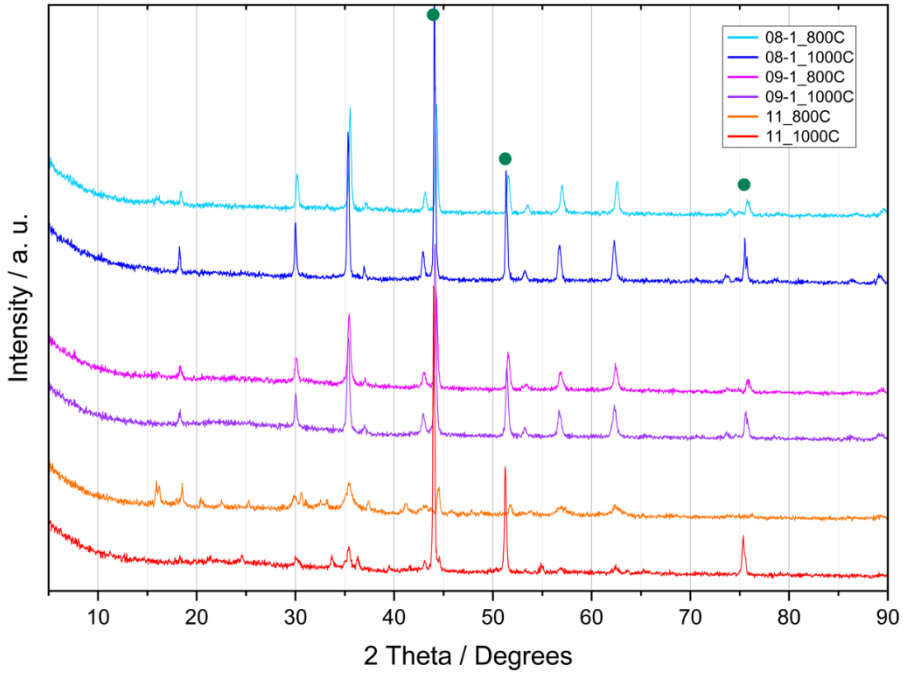

Figure 20 - Powder diffractograms of samples annealed in a tube furnace in an argon atmosphere. Peaks of HEA are marked with green dot. [66]

It seems that the (Cr, Mn, Fe, Co, Ni)C cannot be prepared in a single phase. All the samples contained HEA of the elements and carbide minor phases.

4. 4. Synthesis of CB_4 by UHS

The first step was the optimization of sol-gel synthesis for B_4C preparation. Samples without pH adjustment of the solution before evaporation to gel sublimated during pyrolysis in a tube furnace. The next two batches with various molar ratios of citric acid to boric acid (CA:H_3BO_3) were adjusted to pH 8 and 11 using ammonia. The increase of pH of the homogenous solution (before evaporation) prevented the sublimation. Since there was no difference between the two pH modifications, we decided to continue with pH = 8. Powder diffractograms of all pyrolyzed samples with various molar ratios reaching from 0.1:1 to 1:1 are shown in Figure 21. The sharp peaks at circa 15 ° and 28 ° of 2θ belong to boron oxide. The broad diffraction peak at 25 ° is characteristic for amorphous carbon created by pyrolysis of CA.

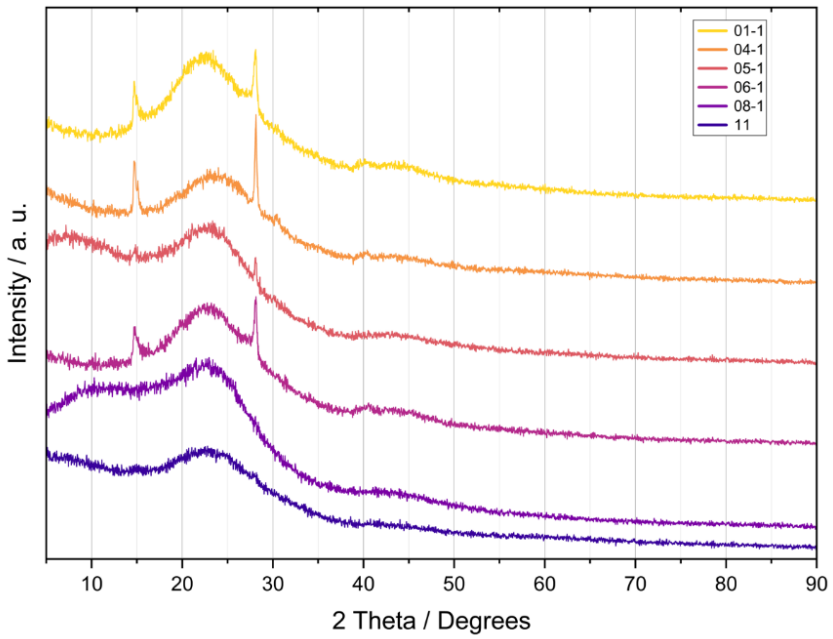

Figure 21 - Powder diffractograms of pyrolyzed samples with adjustment of pH 8 with various molar ratios of CA:H_3BO_3.

Figure 22 shows SEM micrographs of the pyrolyzed sample of CA and H_3BO_3 with pH adjustment at 8. The glass-like structure can be observed.

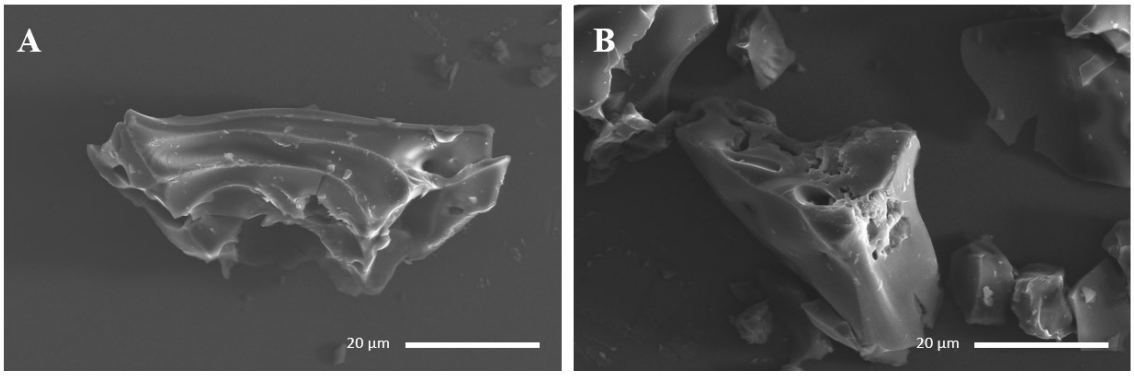

Figure 22 - SEM photos of pyrolyzed mixture of citric acid and boric acid at 600 °C with molar ratio 1:1.

For comparison, Figure 23 presents pyrolyzed gel at 800 °C with a molar ratio CA:H_3BO_3 equal to 0.8:1, which shows the bubbles of CO/CO_2 escaping from the material with high viscosity. It seems that active carbon and boron oxide form a mixed glass. No crystal domains were found for sample treated at 800 °C by TEM.

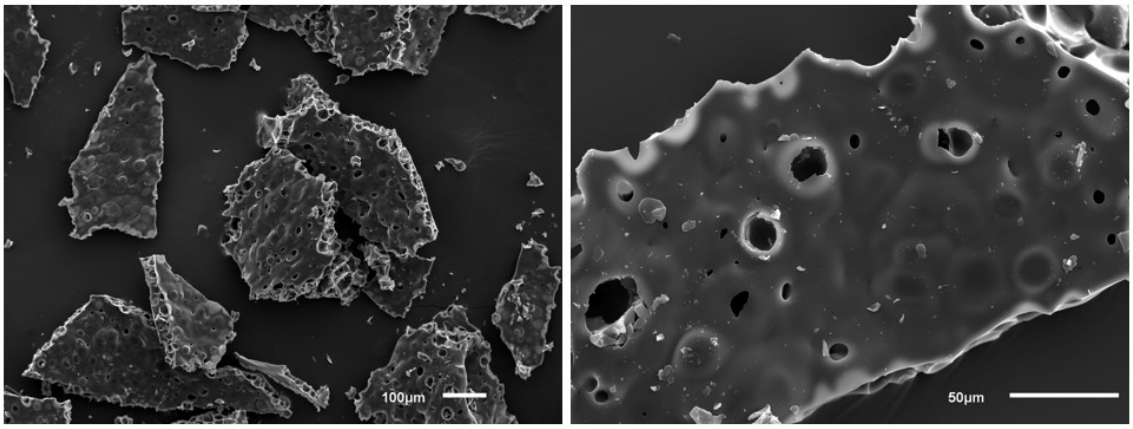

Figure 23 - SEM of pyrolyzed gel with molar ratio CA:H_3BO_3 = 0.8:1

Overall, the boro-carbothermal reduction was observed but the reaction was not complete. Powder diffractograms of the successful sample are in Figure 24. A longer calcination period is needed to complete boro-carbothermal reduction. Our UHS chamber is unsuitable for exposure to ultrahigh temperatures for a longer time. The reference peaks of B_4C are from (PDF 035-0798) and the most intensive peaks are at 35° and 38° of 2θ. The broad peaks of amorphous matter correspond to unreacted reactants.

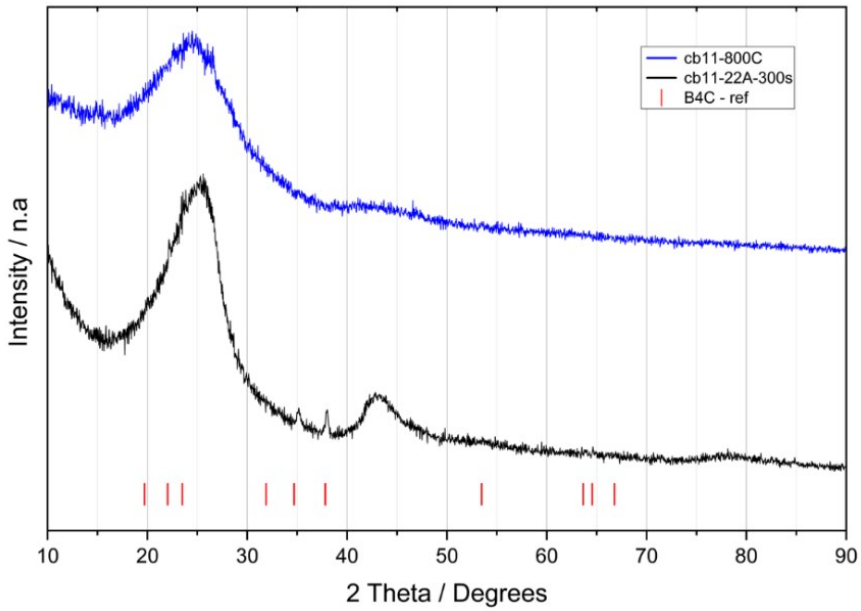

Figure 24 - Powder diffractogram of successfully prepared B_4C with UHS with a molar ratio of CA:H_3BO_3 = 1:1. The pyrolyzed sample at 600 °C (blue), annealed sample with 22 A for 300 s in UHS set-up (black) and the reference position of peaks of B_4C (red).

The SEM micrographs of the product containing B_4C are in Figure 25. The microstructure of the UHS calcined sample changed significantly compared to 800 °C intermediate.

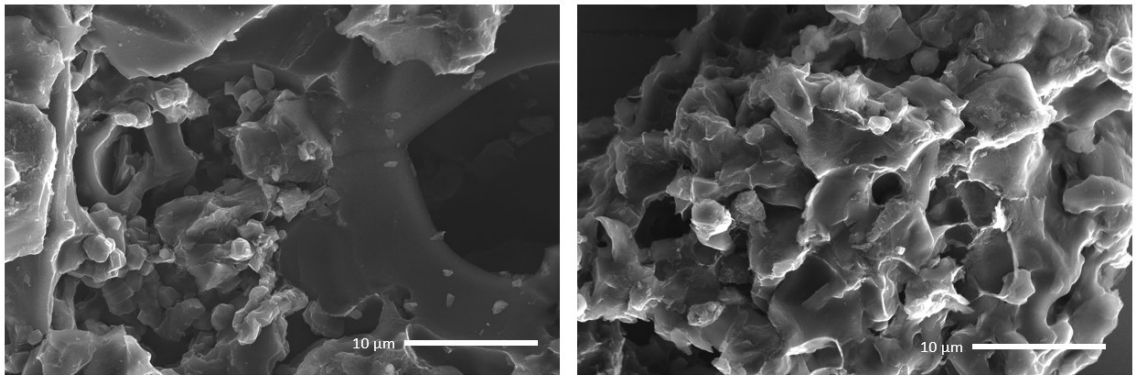

Figure 25 - SEM photos of B_4C crystals (circled) containing samples annealed with 22 A for 300 s.

Figure 26 shows the selection of scanning transmission electron micrographs with details of the nanocrystalline B_4C domains with needle like morphology. These are embedded in the porous active carbon matrix.

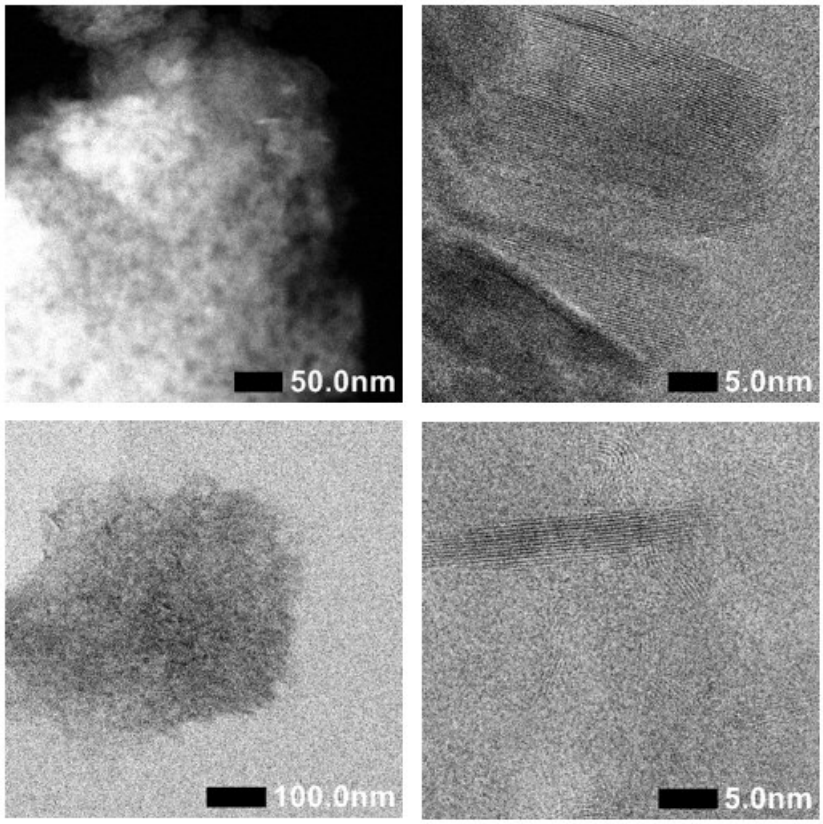

Figure 26 - Scanning transmission electron microscopy of sample annealed with 22 A for 300 s, overall views are on the left and detailed looks on the B_4C nanocrystalline domains are on the left.

5 Conclusion

The main motivation of this thesis was to explore new synthetic routes of HEC materials with focus on the reduction of energy consumption. It was shown that the carbothermal and boro-carbothermal reduction can be performed using the UHS system which assures significant energy savings.

After the successful construction and testing of the apparatus for Ultrafast high-temperature sintering, the modification of three syntheses was accomplished. The experimental approach was similar for all the three synthetic parts: the preparation of homogenous gel by sol-gel method followed by pyrolysis and finished by annealing in UHS apparatus.

Firstly, the HEC with Ti, Zr, Hf, Nb and Ta was prepared. According to PXRD, the synthesised carbide was slightly contaminated with a second phase. This problem could be solved with higher carbon content during carbothermal reduction. Hence, further adjustments to the synthesis need to be done.

Secondly, the carbothermal reduction of Cr, Mn, Fe, Co and Ni was also tested using similar synthesis approach. The major phase of the final samples was high entropy alloy of mentioned elements, and carbide was not observed as a single phase. The sample with higher carbon content (C:M = 2:1) was compared with PDF cards of single carbides. According to PXRD, there is no predominant carbide phase in this sample. Since no HEC of these metals is not mentioned in recent literature and was not observed in presented experiments, its existence can be questioned.

Finally, the synthesis of B_4C was successfully conducted in UHS by reduction of boron oxide by active carbon. However, the set-up used in this thesis could not withstand such high temperatures for a longer time. More resistant setup would be needed to perform complete reduction of the samples.

6 References

[1] Q. Sun *et al.*, "Single-phase (Hf-Mo-Nb-Ta-Ti)C high-entropy ceramic: A potential high temperature anti-wear material," *Tribol Int*, vol. 157, p. 106883, May 2021, doi: 10.1016/j.triboint.2021.106883.

[2] L. Feng, W. G. Fahrenholtz, and D. W. Brenner, "High-Entropy Ultra-High-Temperature Borides and Carbides: A New Class of Materials for Extreme Environments," 2021, doi: 10.1146/annurev-matsci-080819.

[3] E. Castle, T. Csanádi, S. Grasso, J. Dusza, and M. Reece, "Processing and Properties of High-Entropy Ultra-High Temperature Carbides," *Sci Rep*, vol. 8, no. 1, p. 8609, Dec. 2018, doi: 10.1038/S41598-018-26827-1.

[4] M. M. Opeka, I. G. Talmy, E. J. Wuchina, J. A. Zaykoski, and S. J. Causey, "Mechanical, Thermal, and Oxidation Properties of Refractory Hafnium and zirconium Compounds," *J Eur Ceram Soc*, vol. 19, no. 13–14, pp. 2405–2414, 1999, doi: 10.1016/S0955-2219(99)00129-6.

[5] J. W. Yeh, "Recent progress in high-entropy alloys," *Annales de Chimie: Science des Materiaux*, vol. 31, no. 6, pp. 633–648, Nov. 2006, doi: 10.3166/ACSM.31.633-648.

[6] J. W. Yeh *et al.*, "Formation of simple crystal structures in Cu-Co-Ni-Cr-Al-Fe-Ti-V alloys with multiprincipal metallic elements," *Metall Mater Trans A Phys Metall Mater Sci*, vol. 35 A, no. 8, pp. 2533–2536, 2004, doi: 10.1007/S11661-006-0234-4/METRICS.

[7] J. W. Yeh *et al.*, "Nanostructured high-entropy alloys with multiple principal elements: Novel alloy design concepts and outcomes," *Adv Eng Mater*, vol. 6, no. 5, pp. 299–303, 2004, doi: 10.1002/ADEM.200300567.

[8] E. Castle, T. Csanádi, S. Grasso, J. Dusza, and M. Reece, "Processing and Properties of High-Entropy Ultra-High Temperature Carbides," *Scientific Reports 2018 8:1*, vol. 8, no. 1, pp. 1–12, Jun. 2018, doi: 10.1038/s41598-018-26827-1.

[9] S. Barbarossa, R. Orrù, S. Garroni, R. Licheri, and G. Cao, "Ultra high temperature high-entropy borides: Effect of graphite addition on oxides removal and densification behaviour," *Ceram Int*, vol. 47, no. 5, pp. 6220–6231, Mar. 2021, doi: 10.1016/J.CERAMINT.2020.10.200.

[10] T. Jin *et al.*, "Mechanochemical-Assisted Synthesis of High-Entropy Metal Nitride via a Soft Urea Strategy," *Advanced Materials*, vol. 30, no. 23, p. 1707512, Jun. 2018, doi: 10.1002/ADMA.201707512.

[11] C. M. Rost *et al.*, "Entropy-stabilized oxides," *Nature Communications 2015 6:1*, vol. 6, no. 1, pp. 1–8, Sep. 2015, doi: 10.1038/ncomms9485.

[12] W. G. Fahrenholtz and G. E. Hilmas, "Ultra-high temperature ceramics: Materials for extreme environments," *Scr Mater*, vol. 129, pp. 94–99, Mar. 2017, doi: 10.1016/J.SCRIPTAMAT.2016.10.018.

[13] H. Chen *et al.*, "Entropy-stabilized metal oxide solid solutions as CO oxidation catalysts with high-temperature stability," *J Mater Chem A Mater*, vol. 6, no. 24, pp. 11129–11133, Jun. 2018, doi: 10.1039/C8TA01772G.

[14] J. L. Braun *et al.*, "Charge-Induced Disorder Controls the Thermal Conductivity of Entropy-Stabilized Oxides," *Advanced Materials*, vol. 30, no. 51, p. 1805004, Dec. 2018, doi: 10.1002/ADMA.201805004.

[15] A. Vladescu *et al.*, "In Vitro Biocompatibility of Si Alloyed Multi-Principal Element Carbide Coatings," *PLoS One*, vol. 11, no. 8, p. e0161151, Aug. 2016, doi: 10.1371/JOURNAL.PONE.0161151.

[16] V. Braic, M. Balaceanu, M. Braic, A. Vladescu, S. Panseri, and A. Russo, "Characterization of multi-principal-element (TiZrNbHfTa)N and (TiZrNbHfTa)C coatings for biomedical applications," *J Mech Behav Biomed Mater*, vol. 10, pp. 197–205, Jun. 2012, doi: 10.1016/J.JMBBM.2012.02.020.

[17] B. Cantor, I. T. H. Chang, P. Knight, and A. J. B. Vincent, "Microstructural development in equiatomic multicomponent alloys," *Materials Science and Engineering: A*, vol. 375–377, no. 1-2 SPEC. ISS., pp. 213–218, Jul. 2004, doi: 10.1016/J.MSEA.2003.10.257.

[18] J. W. Yeh *et al.*, “Nanostructured high-entropy alloys with multiple principal elements: Novel alloy design concepts and outcomes,” *Adv Eng Mater*, vol. 6, no. 5, pp. 299–303, 2004, doi: 10.1002/ADEM.200300567.

[19] M. H. Tsai and J. W. Yeh, “High-entropy alloys: A critical review,” *Mater Res Lett*, vol. 2, no. 3, pp. 107–123, 2014, doi: 10.1080/21663831.2014.912690.

[20] P. Šolcová *et al.*, “Preparation of High-Entropy (Ti, Zr, Hf, Ta, Nb) Carbide Powder via Solution Chemistry,” *Inorg Chem*, vol. 60, no. 11, 2021, doi: 10.1021/acs.inorgchem.1c00776.

[21] Y. Z. Y. W. G. C. YJ Zhou, “Solid solution alloys of AlCoCrFeNiTix with excellent room-temperature mechanical properties,” *Appl. Phys. Lett.*, vol. 90, p. 181904, 2007.

[22] C. J. Tong *et al.*, “Microstructure characterization of AlxCoCrCuFeNi high-entropy alloy system with multiprincipal elements,” *Metall Mater Trans A Phys Metall Mater Sci*, vol. 36, no. 4, pp. 881–893, 2005, doi: 10.1007/S11661-005-0283-0/METRICS.

[23] K. Jin and H. Bei, “Single-phase concentrated solid-solution alloys: Bridging intrinsic transport properties and irradiation resistance,” *Front Mater*, vol. 5, p. 26, Apr. 2018, doi: 10.3389/FMATS.2018.00026/BIBTEX.

[24] E. P. George, D. Raabe, and R. O. Ritchie, “High-entropy alloys,” *Nature Reviews Materials 2019 4:8*, vol. 4, no. 8, pp. 515–534, Jun. 2019, doi: 10.1038/s41578-019-0121-4.

[25] J. W. Yeh, Y. L. Chen, S. J. Lin, and S. K. Chen, “High-Entropy Alloys – A New Era of Exploitation,” *Materials Science Forum*, vol. 560, pp. 1–9, Nov. 2007, doi: 10.4028/WWW.SCIENTIFIC.NET/MSF.560.1.

[26] H. Itoh, H. Arashima, K. Kubo, T. Kabutomori, and K. Ohnishi, “Improvement of cyclic durability of BCC s tructured Ti-Cr-V alloys,” *J Alloys Compd*, vol. 404–406, no. SPEC. ISS., pp. 417–420, Dec. 2005, doi: 10.1016/j.jallcom.2004.12.175.

[27] J. Montero, G. Ek, M. Sahlberg, and C. Zlotea, “Improving the hydrogen cycling properties by Mg addition in Ti-V-Zr-Nb refractory high entropy alloy,” *Scr Mater*, vol. 194, p. 113699, Mar. 2021, doi: 10.1016/J.SCRIPTAMAT.2020.113699.

[28] J. Gild *et al.*, “High-Entropy Metal Diborides: A New Class of High-Entropy Materials and a New Type of Ultrahigh Temperature Ceramics OPEN,” *Nature Publishing Group*, 2016, doi: 10.1038/srep37946.

[29] A. Kirnbauer *et al.*, “Thermal stability and mechanical properties of sputtered (Hf,Ta,V,W,Zr)-diborides,” *Acta Mater*, vol. 200, pp. 559–569, Nov. 2020, doi: 10.1016/j.actamat.2020.09.018.

[30] Y. Zhang *et al.*, “Microstructure and mechanical properties of high-entropy borides derived from boro/carbothermal reduction,” *J Eur Ceram Soc*, vol. 39, no. 13, pp. 3920–3924, Oct. 2019, doi: 10.1016/J.JEURCERAMSOC.2019.05.017.

[31] R. D. KOESTER and D. P. MOAK, “Hot Hardness of Selected Borides, Oxides, and Carbides to 1900°C,” *Journal of the American Ceramic Society*, vol. 50, no. 6, pp. 290–296, Jun. 1967, doi: 10.1111/J.1151-2916.1967.TB15112.X.

[32] W. G. Fahrenholtz, G. E. Hilmas, I. G. Talmy, and J. A. Zaykoski, “Refractory Diborides of Zirconium and Hafnium,” *Journal of the American Ceramic Society*, vol. 90, no. 5, pp. 1347–1364, May 2007, doi: 10.1111/J.1551-2916.2007.01583.X.

[33] B. Storr *et al.*, “Properties of high entropy borides synthesized via microwave-induced plasma,” *APL Mater*, vol. 10, no. 6, p. 061109, Jun. 2022, doi: 10.1063/5.0098276.

[34] L. Feng, W. G. Fahrenholtz, and G. E. Hilmas, “Processing of dense high-entropy boride ceramics,” *J Eur Ceram Soc*, vol. 40, no. 12, pp. 3815–3823, Sep. 2020, doi: 10.1016/J.JEURCERAMSOC.2020.03.065.

[35] E. Chicardi, C. García-Garrido, J. Hernández-Saz, and F. J. Gotor, “Synthesis of all equiatomic five-transition metals High Entropy Carbides of the IVB (Ti, Zr, Hf)

and VB (V, Nb, Ta) groups by a low temperature route," *Ceram Int*, vol. 46, no. 13, pp. 21421–21430, Sep. 2020, doi: 10.1016/j.ceramint.2020.05.240.

[36] J. Dusza *et al.*, "Microstructure of (Hf-Ta-Zr-Nb)C high-entropy carbide at micro and nano/atomic level," *J Eur Ceram Soc*, vol. 38, no. 12, pp. 4303–4307, Sep. 2018, doi: 10.1016/j.jeurceramsoc.2018.05.006.

[37] X. Han *et al.*, "Improved creep resistance of high entropy transition metal carbides," *J Eur Ceram Soc*, vol. 40, no. 7, pp. 2709–2715, Jul. 2020, doi: 10.1016/J.JEURCERAMSOC.2019.12.036.

[38] E. Castle, T. Csanádi, S. Grasso, J. Dusza, and M. Reece, "Processing and Properties of High-Entropy Ultra-High Temperature Carbides," *Sci Rep*, vol. 8, no. 1, pp. 1–12, Dec. 2018, doi: 10.1038/s41598-018-26827-1.

[39] S. A. Ghaffari, M. A. Faghihi-Sani, F. Golestani-Fard, and M. Nojabayy, "Diffusion and solid solution formation between the binary carbides of TaC, HfC and ZrC," *Int J Refract Metals Hard Mater*, vol. 41, pp. 180–184, Nov. 2013, doi: 10.1016/j.ijrmhm.2013.03.009.

[40] H. J. Emeléus, *Advances in Inorganic Chemistry and Radiochemistry - Knihy Google*. 1968. Accessed: Apr. 04, 2023. [Online]. Available: https://books.google.cz/books?id=-SnCsg5jM_kC&pg=PA169&redir_esc=y#v=onepage&q&f=false

[41] O. Cedillos-Barraza *et al.*, "Investigating the highest melting temperature materials: A laser melting study of the TaC-HfC system," *Sci Rep*, vol. 6, 2016, doi: 10.1038/srep37962.

[42] P. Sarker *et al.*, "High-entropy high-hardness metal carbides discovered by entropy descriptors," *Nat Commun*, vol. 9, no. 1, pp. 1–10, Dec. 2018, doi: 10.1038/s41467-018-07160-7.

[43] E. Wuchina, E. Opila, M. Opeka, W. Fahrenholtz, and I. Talmy, "UHTCs: Ultra-High Temperature Ceramic Materials for Extreme Environment Applications."

[44] X. Yan, L. Constantin, Y. Lu, J. F. Silvain, M. Nastasi, and B. Cui, "(Hf0.2Zr0.2Ta0.2Nb0.2Ti0.2)C high-entropy ceramics with low thermal conductivity," *Journal of the American Ceramic Society*, vol. 101, no. 10, pp. 4486–4491, Oct. 2018, doi: 10.1111/jace.15779.

[45] J. Zhou, J. Zhang, F. Zhang, B. Niu, L. Lei, and W. Wang, "High-entropy carbide: A novel class of multicomponent ceramics," *Ceram Int*, vol. 44, no. 17, pp. 22014–22018, Dec. 2018, doi: 10.1016/j.ceramint.2018.08.100.

[46] X.-F. Wei *et al.*, "High-entropy carbide ceramics with refined microstructure and enhanced thermal conductivity by the addition of graphite," *J Eur Ceram Soc*, Mar. 2021, doi: 10.1016/j.jeurceramsoc.2021.03.053.

[47] W. G. Fahrenholtz and G. E. Hilmas, "Ultra-high temperature ceramics: Materials for extreme environments," *Scr Mater*, vol. 129, pp. 94–99, Mar. 2017, doi: 10.1016/j.scriptamat.2016.10.018.

[48] D. Salvato *et al.*, "Innovative preparation route for uranium carbide using citric acid as a carbon source," 2016, doi: 10.1016/j.ceramint.2016.07.138.

[49] B. Matović *et al.*, "Synthesis and characterization of hafnium carbide fine powders," *Ceram Int*, vol. 39, no. 1, pp. 719–723, Jan. 2013, doi: 10.1016/j.ceramint.2012.06.083.

[50] M. D. Sacks, C.-A. Wang, Z. Yang, and A. Jain, "Carbothermal reduction synthesis of nanocrystalline zirconium carbide and hafnium carbide powders using solution-derived precursors," *J Mater Sci*, vol. 39, no. 19, pp. 6057–6066, 2004, doi: 10.1023/B:JMSC.0000041702.76858.a7.

[51] Z. A. Munir, U. Anselmi-Tamburini, and M. Ohyanagi, "The effect of electric field and pressure on the synthesis and consolidation of materials: A review of the spark plasma sintering method," *J Mater Sci*, vol. 41, no. 3, pp. 763–777, Feb. 2006, doi: 10.1007/S10853-006-6555-2/METRICS.

[52] S. Molina-Molina *et al.*, "A novel Multi-Phase Flash Sintering (MPFS) technique for 3D complex-shaped ceramics," *Appl Mater Today*, vol. 26, p. 101274, Mar. 2022, doi: 10.1016/J.APMT.2021.101274.

[53] G. Cabouro, S. Chevalier, E. Gaffet, Y. Grin, and F. Bernard, “Reactive sintering of molybdenum disilicide by spark plasma sintering from mechanically activated powder mixtures: Processing parameters and properties,” *J Alloys Compd*, vol. 465, no. 1–2, pp. 344–355, Oct. 2008, doi: 10.1016/J.JALLCOM.2007.10.141.

[54] G. Delaizir *et al.*, “A comparative study of Spark Plasma Sintering (SPS), Hot Isostatic Pressing (HIP) and microwaves sintering techniques on p-type Bi2Te3 thermoelectric properties,” *Mater Res Bull*, vol. 47, no. 8, pp. 1954–1960, Aug. 2012, doi: 10.1016/J.MATERRESBULL.2012.04.019.

[55] J. Binner and T. S. R. C. Murthy, “Structural and Thermostructural Ceramics,” *Encyclopedia of Materials: Technical Ceramics and Glasses*, vol. 2–3, pp. 3–24, Jan. 2021, doi: 10.1016/B978-0-12-818542-1.00067-9.

[56] Y. Le Godec and S. Le Floch, “Recent Developments of High-Pressure Spark Plasma Sintering: An Overview of Current Applications, Challenges and Future Directions,” *Materials 2023, Vol. 16, Page 997*, vol. 16, no. 3, p. 997, Jan. 2023, doi: 10.3390/MA16030997.

[57] C. Wang *et al.*, “Rapid Synthesis and Sintering of Metals from Powders,” *Advanced Science*, vol. 8, no. 12, Jun. 2021, doi: 10.1002/ADVS.202004229.

[58] C. Wang *et al.*, “A general method to synthesize and sinter bulk ceramics in seconds,” *Science (1979)*, vol. 368, no. 6490, pp. 521–526, May 2020, doi: 10.1126/SCIENCE.AAZ7681.

[59] R. F. Guo, H. R. Mao, Z. T. Zhao, and P. Shen, “Ultrafast high-temperature sintering of bulk oxides,” *Scr Mater*, vol. 193, pp. 103–107, Mar. 2021, doi: 10.1016/J.SCRIPTAMAT.2020.10.045.

[60] A. Alemayehu *et al.*, “Ultrafast high-temperature sintering of gadolinia-doped ceria,” *J Eur Ceram Soc*, Apr. 2023, doi: 10.1016/J.JEURCERAMSOC.2023.04.025.

[61] C. Wang *et al.*, “A general method to synthesize and sinter bulk ceramics in seconds,” *Science (1979)*, vol. 368, no. 6490, pp. 521–526, May 2020, doi: 10.1126/SCIENCE.AAZ7681/SUPPL_FILE/AAZ7681S2.MP4.

[62] T. P. Mishra *et al.*, “Ultra-fast high-temperature sintering of strontium titanate,” *Acta Mater*, vol. 231, p. 117918, Jun. 2022, doi: 10.1016/J.ACTAMAT.2022.117918.

[63] R. F. Guo, H. R. Mao, Z. T. Zhao, and P. Shen, “Ultrafast high-temperature sintering of bulk oxides,” *Scr Mater*, vol. 193, pp. 103–107, Mar. 2021, doi: 10.1016/J.SCRIPTAMAT.2020.10.045.

[64] L. Spiridigliozzi *et al.*, “Ultra-fast high-temperature sintering (UHS) of Ce0.2Zr0.2Y0.2Gd0.2La0.2O2−δ fluorite-structured entropy-stabilized oxide (F-ESO),” *Scr Mater*, vol. 214, p. 114655, Jun. 2022, doi: 10.1016/J.SCRIPTAMAT.2022.114655.

[65] H. R. Mao, E. T. Dong, S. B. Jin, X. M. Qiu, and P. Shen, “Ultrafast high-temperature synthesis and densification of high-entropy carbides,” *J Eur Ceram Soc*, vol. 42, no. 10, pp. 4053–4065, Aug. 2022, doi: 10.1016/J.JEURCERAMSOC.2022.03.054.

[66] T. Nagase *et al.*, “Development of Fe-Co-Cr-Mn-Ni-C high entropy cast iron (HE cast iron) available for casting in air atmosphere,” *Mater Des*, vol. 184, p. 108172, Dec. 2019, doi: 10.1016/J.MATDES.2019.108172.

[67] D. Pankratova, S. M. Giacomelli, K. Yusupov, F. Akhtar, and A. Vomiero, “Co-Cr-Fe-Mn-Ni Oxide as a Highly Efficient Thermoelectric High-Entropy Alloy,” *ACS Omega*, vol. 8, no. 16, Apr. 2023, doi: 10.1021/ACSOMEGA.2C08278.